SIViP
DOI 10.1007/s11760-011-0216-x

ORIGINAL PAPER

Three-dimensional noisy image restoration using filtered extrapolation and deconvolution

Moacir P. Ponti-Jr · Nelson D. A. Mascarenhas · Paulo J. S. G. Ferreira · Claudio A. T. Suazo

Received: 4 December 2009 / Revised: 1 February 2011 / Accepted: 2 February 2011

Abstract The problem of restoration in fluorescence microscopy has to deal at the same time with blurring and photon noise. Their combined effects corrupt the image by inserting elements that do not belong to the real object and distort the contrast. This hinders the possibility of using the images for visualization, recognition, and analysis using the three-dimensional data. The algorithms developed to restore the lost frequencies and perform band extrapolation, in general, assume absence of noise or an additive noise. This paper presents a restoration approach through band extrapolation and deconvolution that deals with the noise. An extrapolation algorithm using constraints on both spatial and frequency domains with a smoothing operator were combined with the Richardson-Lucy iterative algorithm. The results of the method for simulated data are compared with those obtained by the original Richardson-Lucy algorithm and also regularized by Total Variation. The extrapolation of frequencies is also analyzed both in synthetic and in real images. The method improved the results with higher signal-to-noise ratio and quality index values, performing band extrapolation, and achieving a better visualization of the 3D structures.

Keywords Image restoration · Computational optical sectioning microscopy · Filtered extrapolation

This study was partially supported by CAPES with a PhD/PDEE scolarship.

M. P. Ponti-Jr (✉)
Institute of Mathematical and Computer Sciences,
University of São Paulo, São Carlos, SP 13560-970, Brazil
e-mail: moacir@icmc.usp.br

N. D. A. Mascarenhas · C. A. T. Suazo
Universidade Federal de São Carlos, São Carlos,
SP 13565-905, Brazil
e-mail: nelson@dc.ufscar.br

C. A. T. Suazo
e-mail: claudio@ufscar.br

P. J. S. G. Ferreira
Signal Processing Laboratory, IEETA—Universidade de Aveiro,
Aveiro 3810-193, Portugal
e-mail: pjf@ua.pt

1 Introduction

The light microscope is an important tool for medical and biological purposes. The fluorescence microscopy is a particular technique suitable to analyze 3D structures of living biological cells and tissues and assess the viability of cell cultures [30]. Applications include the report of virus infections, disease diagnosis, cancer research, and other applications, specially after the development of new fluorescent proteins [21]. With the advent of potential applications of light microscopy in medicine, biotechnology and related fields is important to study possibilities of resolution improvement [6].

Although the practical importance of the optical fluorescence microscopy cannot be denied, Fourier optics demonstrates that there exists a cut-off spatial frequency determined by the shape and size of the optical system lenses and acquisition conditions [15]. This distortion of the frequency components is governed by the OTF (Optical Transfer Function), the normalized Fourier transform of the PSF (Point Spread Function) of the imaging system. Besides, the presence of noise—well modeled by a Poisson distribution—is another distortion caused by the often low exposure acquisition time.

The algorithms that allow a reconstruction of the distorted images and the recovery of frequencies lost in the

Published online: 22 February 2011

acquisition process are part of image restoration methods and are often called band extrapolation algorithms. Although deconvolution algorithms belong to a different class, some deconvolution algorithms are able to perform band extrapolation. A probabilistic algorithm was developed by Richardson [29] and Lucy [22] to restore images using a Poisson process to model the image formation system. At the time those papers were written, the ability to restore frequencies beyond the signal passband was controversial [1]. However, Gerchberg [13] and Papoulis [24] showed that the use of known constraints on frequency and time domains could extrapolate signals. Later, the same algorithm was analyzed for the discrete case [9]. The limits of the band extrapolation lies on the prior knowledge available and the presence of noise [32].

The band extrapolation capability of the Expectation-Maximization algorithm, equivalent to the Richardson-Lucy algorithm for a Poisson distribution, was studied in [5]. The authors noted an increase in the practical bandwith subject to the use of non-linear restoration algorithms. In another related study, Danuser [6] imposed prior knowledge through geometric and dynamic models of the scene. A POCS-Taylor expansion extrapolation algorithm, assuming noiseless data, was also proposed [2]. A Bayesian reconstruction based on edge information was also developed [7].

Since the presence of noise in images represents a limit for extrapolation [18,32], some papers investigated the prefiltering of 3D microscopy images [4,19] and a regularization based on Total Variation [8]. The Total Variation is an interesting approach, since it can perform extrapolation of frequencies [23]. Recent advances in deconvolution includes a blind deconvolution algorithm that models the space of PSFs through machine learning techniques [20], an alternate direction optimization [10], and a scaled gradient projection method to speed up convergence [3].

In this study, we propose a combination of the best features of Gerchberg-Papoulis (G-P) and Richardson-Lucy (R-L) algorithms with a filtering step between the iterations. The filtering is carried out only at the extrapolated frequencies and the known portion is re-inserted after filtering. This procedure uses constraints of G-P algorithm while preventing the noise amplification without oversmoothing the signal. A previous work applied a simple combination of Richardson-Lucy and the Gerchberg-Papoulis for 2D images [27]. However, it did not consider realistic images and their three-dimensional aspects. It also did not study the band extrapolation capabilities of the method.

Our goal is to obtain simultaneous restoration and extrapolation. The main contribution is to show that it can be achieved with the use of an iterative filtered extrapolation combined with deconvolution, overcoming some of the difficulties that exist when going beyond the diffraction limit in the presence of noise.

2 3D microscopy image restoration

The 3D microscopy image reconstruction is carried out by acquiring 2D images on several focal planes. These 2D images (slices of a specimen) are stacked to generate a 3D image (Fig. 1). This method is often called COSM (computational optical sectioning microscopy). Images acquired using this method have an out-of-focus blur due to the optical characteristics of the microscopy. The wide-field microscope uses an excitation light that illuminates the whole specimen, so that the camera captures light coming from the focal plane and also from the planes above and below, yielding an out-of-focus, blurred image. This effect causes the wide-field microscopy to obtain degraded 3D images. It is important to observe that the wide-field microscope is very different from the confocal microscope with respect to the blurring and noise (as can be seen in Fig. 2).

The general imaging system for an optical wide-field microscope can be modeled by considering the object to be imaged as a function $f(x, y, z)$ in the 3D real space, where (x, y, z) are the coordinates of the space. Each image obtained belongs to a different focal plane along the z-axis. Due to the photon counting nature of light-based sensors, the main source of noise is a signal-dependent noise and can

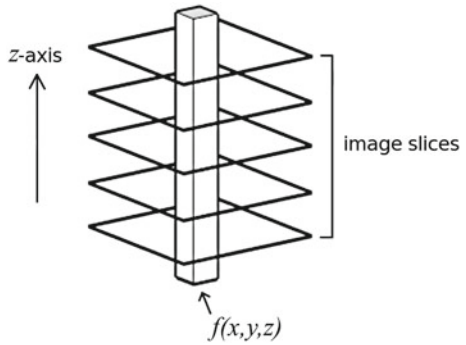

Fig. 1 A representation of 2D image slices acquisition of a specimen function in order to reconstruct a 3D image

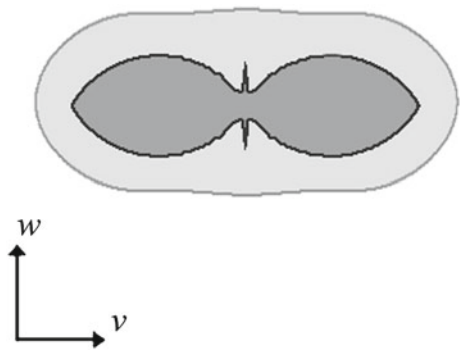

Fig. 2 Comparison of contour lines of the OTF frequency support of wide-field (*dark gray*) and confocal microscopes (*light gray*)

be well modeled by a Poisson distribution. Considering each value of the function $g(x, y, z)$ to be a realization of a random variable described by a Poisson process, the model can be written as:

$$g(x, y, z) = \mathcal{P}\{f(x, y, z) * h(x, y, z)\}, \tag{1}$$

where $\mathcal{P}\{\}$ represents a Poisson process, producing a noise that is correlated with $f(x, y, z) * h(x, y, z)$. The additive noise is not significant when compared to the Poisson noise, so it can be neglected for simplification purposes. Nevertheless, for images with high signal-to-noise ratio, it is possible to approximate the noise by an additive Gaussian noise [34].

The most natural solution for this problem would be the inverse filter. Unfortunately, practical OTF have zero-valued regions. Indeed, Philip [25] and Sheppard et al. [33] showed that the practical support of the OTF is a well-defined set occupying only a small fraction of the whole discrete Discrete Fourier Transform array. Figure 2 shows the OTF frequency domain support of both confocal and wide-field microscopes, to illustrate the effect on low and high-frequencies along the w axis in wide-field microscopy. Besides the frequency band-limit, the OTF low amplitude regions would also cause noise amplification. So, under these conditions the inverse filter does not exist.

Another important effect in fluorescence microscopy is called photobleaching [35]. The specimen is steined with a fluorochrome that allow the tissues to produce light. However, the fluorescence decay is often exponential, so the intensities captured by the microscope decrease from one acquired slice to another. Software solutions exist to take into account this difficulty, but practical procedures to reduce this effect include the acquisition of less images in the z direction and the reduction of the exposure time.

3 Richardson-Lucy algorithm

The Richardson-Lucy (R-L) algorithm uses a probabilistic approach: given a degraded image g, what is the image f that maximizes the probability of observing the image g? Considering the image as an observation of a poisson process, the likelihood function would be:

$$p(g|f) = \prod_{\mathbf{x}} \frac{h(\mathbf{x}) * f(\mathbf{x})^{g(\mathbf{x})} e^{-h(\mathbf{x})*f(\mathbf{x})}}{g(\mathbf{x})!}, \tag{2}$$

where $\mathbf{x}$ represents (x, y, z) for a 3D signal. From this equation, a functional to be minimized, $L(\hat{f}) = -\log p(g|f)$ is obtained, giving the maximum likelihood estimation:

$$L(\hat{f}) = \sum_{\mathbf{x}} -g(\mathbf{x}) \log\left[(h * \hat{f})(\mathbf{x})\right] + (h * \hat{f})(\mathbf{x}). \tag{3}$$

An iterative algorithm can be derived from the above functional. It is called the Richardson-Lucy algorithm and it is given by:

$$\hat{f}_{n+1}(\mathbf{x}) = \left[\left(\frac{g(\mathbf{x})}{\hat{f}_n(\mathbf{x}) * h(\mathbf{x})}\right) * h(\mathbf{x})\right] \times \hat{f}_n(\mathbf{x}). \tag{4}$$

This algorithm stops after a finite number of iterations. When the deconvolution is ill-posed, a common situation in real applications, the signal-to-noise ratio becomes increasingly poorer as the number of iterations $n \to \infty$.

4 Gerchberg-Papoulis algorithm

The Gerchberg-Papoulis (G-P) algorithm assumes that there is some knowledge about the bandwidth and iteratively imposes the requirements that the signal is band-limited and matches the known portion of the signal. Let $g(\mathbf{x})$ have a spectrum $G(\mathbf{u})$ and Ω the region where $G(\mathbf{u})$ is non-zero, $\mathbf{u}$ represents (u, v, w) for a 3D signal in the frequency domain.

Since $g(\mathbf{x})$ is known within a region T, since it is space limited, the spatial support can be defined as:

$$B_T(\mathbf{x}) = \begin{cases} 1, & \mathbf{x} \in T \\ 0, & \mathbf{x} \notin T \end{cases} \tag{5}$$

The spectral pupil can be defined in the same context:

$$B_\Omega(\mathbf{u}) = \begin{cases} 1, & \mathbf{u} \in \Omega \\ 0, & \mathbf{u} \notin \Omega \end{cases} \tag{6}$$

The algorithm consists in imposing the constraints above, as follows;

$$\begin{aligned} \hat{e}_0(\mathbf{x}) &= B_T g(\mathbf{x}), \\ \hat{e}_{n+1}(\mathbf{x}) &= \hat{e}_0 + (1 - B_T) \cdot \mathfrak{F}^{-1}\{B_\Omega E_n(\mathbf{u})\}, \end{aligned} \tag{7}$$

where $\hat{e}_0(\mathbf{x})$ is the first estimation of the extrapolated image, $\hat{e}_{n+1}(\mathbf{x})$ is the estimation at interation $n + 1$, and $\hat{E}_n(\mathbf{u})$ is the current estimation in the frequency domain. The signal is clipped in the frequency domain by the spectral pupil and the known portion of the signal is imposed in the space domain. It constrains the frequencies to extend the spatial limit. The convergence of this method is established in the absence of noise [24].

5 Method

5.1 Filtered Gerchberg-Papoulis

The presence of noise, specially non-additive non-Gaussian noise, can easily led the reconstruction algorithm to diverge after a number of iterations. So, a filtering step can be introduced to reduce the variation in the image and make the restoration and spectrum extrapolation easier. The filtering of data before running a restoration method for a non-linear iterative method was explored by Kempen et al. [19]

and for linear restoration by Colicchio et al. [4], showing good results. To prevent over-smoothing and to preserve the frequencies already present in the observed image, the filtering step can be restricted to the extrapolated frequencies beyond the limit Ω. This represents an attempt to preserve the signal while smoothing the high-frequencies, since the signal information in extrapolated frequencies are often corrupted by noise as pointed by Sementilli et al. [32]. The algorithm that includes the filtering of the extrapolated frequencies can be written as follows:

$$\begin{aligned}\hat{E}_{n+1}(\mathbf{u}) &= B_\Omega \hat{E}_n(\mathbf{u}) + \text{Filter}\left[(1 - B_\Omega) \cdot \mathfrak{F}\left\{B_T \hat{e}_n(\mathbf{x})\right\}\right],\\ \hat{e}_{n+1}(\mathbf{x}) &= \mathfrak{F}^{-1}\left\{\hat{E}_{n+1}\right\},\end{aligned} \tag{8}$$

where $\hat{e}_n(\mathbf{x})$ and $\hat{E}_n(\mathbf{x})$ are the previous estimates of the image and its Fourier transform, respectively. The space support must be wide enough so that the object lies completely on it. The modified algorithm constrains the spatial limit in order to extrapolate the frequency limit. The spatial support constraint is based on the work of Homem et al. [16]. Since the observed images have no well-defined region T, we performed an extension of six voxels in each direction of the image, so an image of size (n, m, o) turns into an image of size $(n+6, m+6, o+6)$. The parameter T is defined to be the region of the image before extension. The edges produced by the image extension are smoothed to avoid artifacts.

The extrapolated portion of the spectrum is filtered and the frequencies within the band-limit are re-inserted. The spectral pupil can be defined as a circular area defined by the frequency boundaries where the spectrum goes approximately to zero, or the practical bandwidth. It is important to observe that the frequencies are not clipped to zero, for this could impede the extrapolation. The operator Filter $[I(\mathbf{u})]$ for the extrapolated frequencies $I(\mathbf{u})$ is performed as follows:

$$\text{Filter}\left[I(\mathbf{u})\right] = \mathfrak{F}\left\{\text{SpFilter}\left[\mathfrak{F}^{-1}\left\{I(\mathbf{u})\right\}\right]\right\}, \tag{9}$$

where SpFilter is a filter defined in the space domain. In this paper, two kinds of filters were used: the mean and the median filters. These were chosen so that we could analyse the effects of the most simple linear (mean) and non-linear (median) filters. The filtering of selected frequency componentes were already explored by Foi et al. [11,12], through local shrinkage of coefficients and Wiener filtering. The rationale behind the use of filters, as pointed out by Restrepo and Chacon [28], Sawicki [31], is that it has smoothing properties that can be used for elimination of impulsive disturbances, and consequently can prevent the generation of undesired artifacts in restoration-extrapolation algorithm.

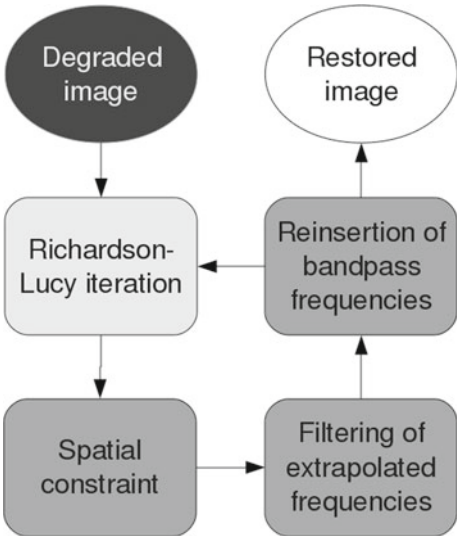

Fig. 3 RL-FGP iterative algorithm diagram

5.2 Restoration-extrapolation algorithm

The proposed method simultaneously applies the R-L algorithm and the G-P algorithm as follows:

$$\begin{aligned}\hat{f}_{n+1} &= \text{RL}\left[e_n\right]\\ \hat{e}_{n+1} &= \text{FGP}\left[f_{n+1}\right],\end{aligned} \tag{10}$$

where RL is the Richardson-Lucy algorithm, and FGP is the Filtered Gerchberg-Papoulis algorihtm, modified to perform band extrapolation with filtering of extrapolated frequencies. The algorithm scheme can also be seen in Fig. 3. The iterations are performed until the residual ε reaches the value 0.001. The residual is defined as:

$$\varepsilon = \frac{\left\|\hat{f}_n - \hat{f}_{n-1}\right\|}{\left\|\hat{f}_{n-1}\right\|} \tag{11}$$

6 Experiments

A series of experiments were carried out using the methods described in the previous sections. Three images were used to test the algorithms, all images with 256 gray levels. The phantom images were convolved with a theoretic microscope PSF. The PSF was constructed following the theoretical model proposed by Gibson and Lanni [14]. Poisson noise was also introduced in the synthetic images—note that the parameter of Poisson distribution represents both the mean number of occurrences and its variance, so that images of lower intensities are more likely to present a poorer signal-to-noise ratio. The data used were similar to that used in the

study of Homem [17]. Additional material can be found at the project website, cited at this paper title page.

The following images were used in the experiments:

1. **Bead phantom image**: with size 128 × 128 × 128, this kind of phantom is often used in deconvolution experiments—a montage of sections of the original and degraded phantom is shown in Fig. 4. The blurring effect in the axial direction is not strong, so we can observe the behavior of the algorithms in a more controlled way. Since the phantom was created with a maximum intensity of 150, its degraded version has a poor signal-to-noise ratio.
2. **Cell phantom image**: with size 256 × 256 × 32, it is a phantom of a simulated cell culture—a montage of sections of the original and degraded phantom is shown in Fig. 5. The PSF parameters were based on the microscope used to acquire the real images and, therefore, the axial blurring effect is stronger.
3. **Real fluorescence images**: two 3D real images obtained with a wide-field fluorescence microscope. The image 1 was acquired under a lower exposure time (1/5 s) when compared with image 2, so image 2 is expected to have a better signal-to-noise ratio—sections of the real images are shown in Fig. 6.
   - Real 1: 256 × 256 × 32 voxels, 20X, 0.45 NA, emission filter $\lambda = 500$ nm, voxel dimension 0.11 × 0.11 × 0.20.
   - Real 2: 128 × 128 × 128 voxels, 20X, 0.75 NA, emission filter $\lambda = 530$ nm, voxel dimension 0.71 × 0.71 × 0.71.

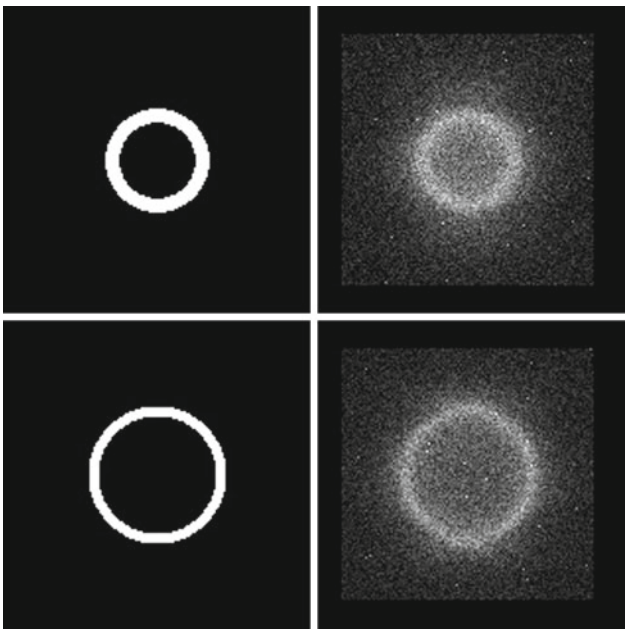

Fig. 4 Sections $(x, 42, z)$ and $(x, 64, z)$ of the original and degraded bead image

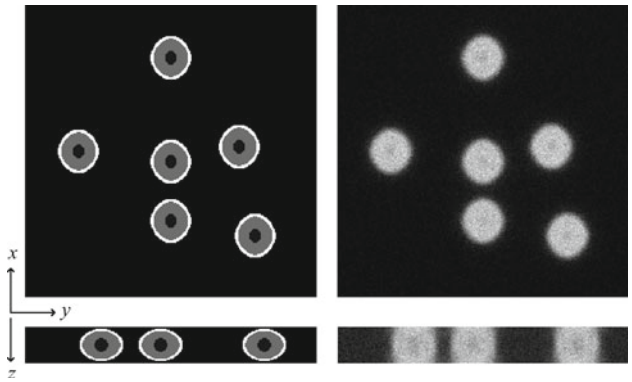

Fig. 5 Sections $(x, y, 16)$ and $(x, 128, z)$ of the original and degraded cells image

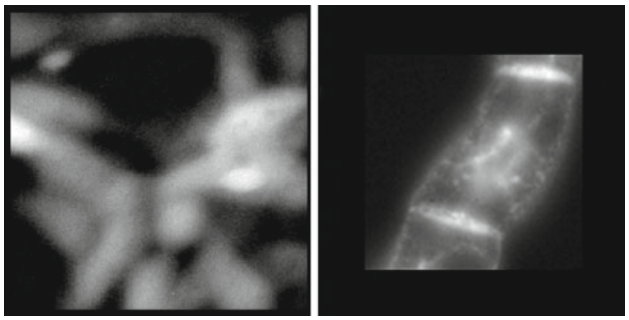

Fig. 6 Sections of the two real images: image 1 $(x, y, 14)$ and image 2 $(x, y, 58)$

The colormap of all images were normalized to a 256 grayscale for visualization.

Both phantom and real images were restored using the R-L algorithm, and the R-L algorithm combined with the filtered G-P, that will be refered as RL-FGP-1 (using a [3 × 3] median filter) and RL-FGP-2 (using a [3 × 3] mean filter). We also restore the images using the R-L with Total Variation regularization algorithm exactly as described in [8]. Different sizes of image spectral support were also used to performing RL-FGP and observe how the method behaves when filtering different range of frequencies.

6.1 Evaluation

The restored images were evaluated by observing ISNR (Improvement on Signal-to-Noise Ratio) and the UIQI (Universal Image Quality Index) [36]. The ISNR is given by:

$$\mathrm{ISNR} = 10 \log_{10} \left\{ \frac{\sum_{\mathbf{x}} \|g(\mathbf{x}) - f(\mathbf{x})\|}{\sum_{\mathbf{x}} \left\| \hat{f}(\mathbf{x}) - f(\mathbf{x}) \right\|} \right\}, \tag{12}$$

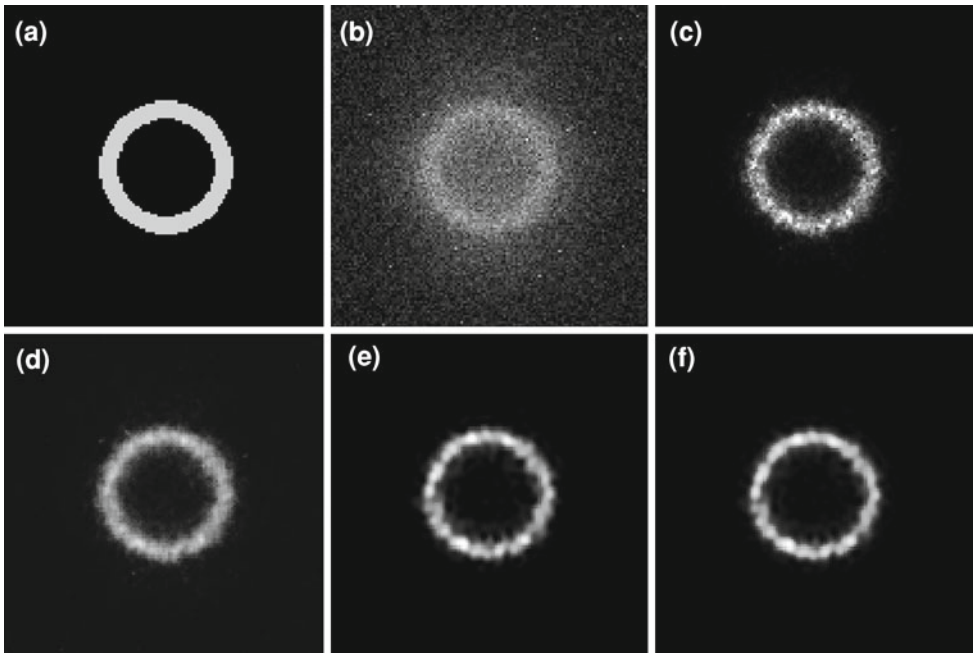

Fig. 7 Sections $(x, 42, z)$ of the best restoration results for the bead image: **a** original, **b** degraded; **c** R-L; **d** RL-TV; **e** RL-FGP-1; **f** RL-FGP-2

where $g(\mathbf{x})$ is the degraded image, $f(\mathbf{x})$ the original image and $\hat{f}(\mathbf{x})$ the restored image. The ISNR compares the degraded and restored images with the original, and yields a number that measures the relative improvement.

The UIQI is given by:

$$\text{UIQI} = \frac{4\sigma_{f\hat{f}} \cdot \overline{f}\,\overline{\hat{f}}}{\left(\sigma_f^2 + \sigma_{\hat{f}}^2\right) \cdot \left(\overline{f}^2 + \overline{\hat{f}}^2\right)}, \tag{13}$$

where letters with bars are averages; $\sigma_{\hat{f}}^2$ and σ_f^2 are the variance of the original and restored images, respectively, and $\sigma_{f\hat{f}}$ is the correlation coefficient between f and $\hat{f}$. The dynamic range of UIQI is $[-1, 1]$. The best value, 1, is achieved if and only if $f = \hat{f}$.

The UIQI is an alternative to the ISNR since it models the image distortion as a combination of loss of correlation, luminance distortion and contrast distortion, comparing the original and processed image. The loss of correlation is related to the band limit, so we expect to observe a higher UIQI for better extrapolated images.

To assess the spectral extrapolation, we also compare the practical passband of the images [5], the region of the frequency domain where the modulus of the Fourier transform is larger than 1% of its peak value. That is, the region where:

$$\left|\hat{F}(\mathbf{u})/\hat{F}(\mathbf{0})\right| > 0.01, \tag{14}$$

By computing the number of coefficients found in the practical passband, it is possible to have a numerical information on how much the algoritms extrapolated the frequencies.

7 Results

The degraded images were restored using the three algorithms described in sect. 6, and the TV regularization parameter λ was experimentally found for each image. The results for the synthetic images are shown in Fig. 7 and Table 1 (bead), Fig. 8 and Table 2 (cell). The restoration of real images are shown in Figs. 9 and 10, and Tables 3 and 4. Both real images were zoomed to allow a more detailed visualization of the results. The colormap was adjusted in all figures to 256 gray levels.

The RL-FGP method obtained better restoration results when compared with the competing methods. This is confirmed by an improvement in the ISNR, UIQI, and the number of observed frequencies (Table 1). The reason why Total Variation regularization did not perform well was probably because it is based on a gradient edge detector. For confocal microscope images, as used in [8], the edges can be better detected, but in wide-field microscopy images the object boundaries are probably too smooth to obtain a good edge estimation. For the real image 1

Table 1 Bead image restoration evaluation

Images	ISNR	UIQI	#Passband	#Iter.
Degraded image	–	0.37	449	–
RL	5.26	0.68	13245	190
RL-TV $\lambda = 0.004$	7.05	0.71	13075	414
RL-FGP-1 (median)	7.41	0.76	16921	375
RL-FGP-2 (mean)	7.39	0.75	16035	368

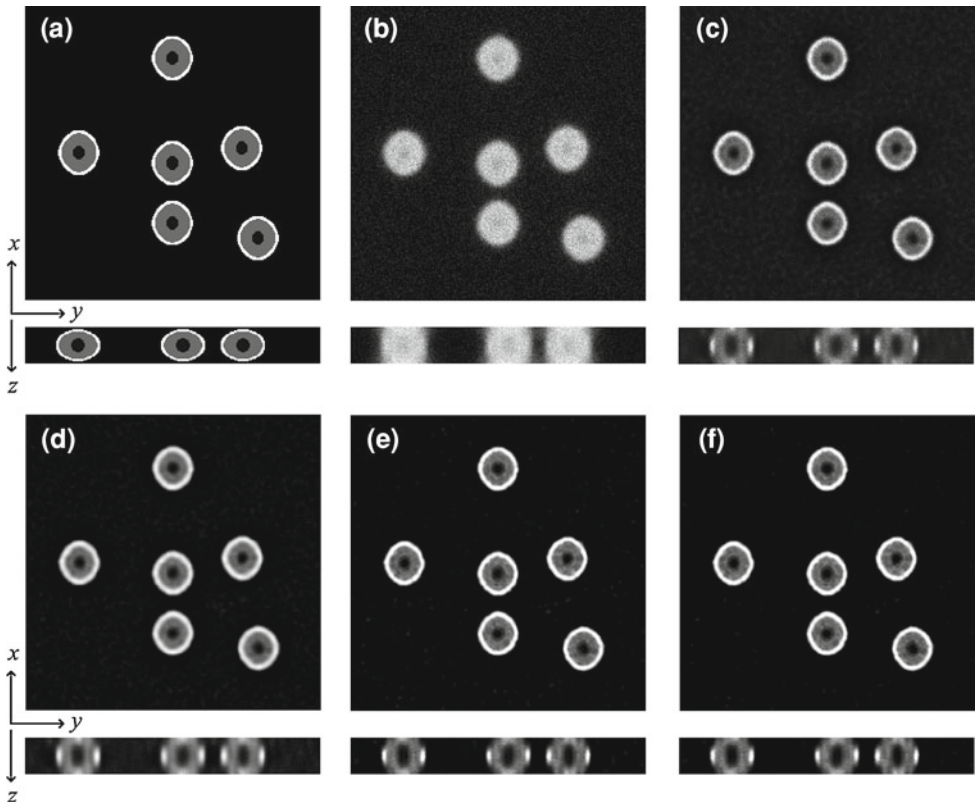

Fig. 8 Sections $(x, y, 16)$ and $(x, 128, z)$ of the best restoration results for the cells image: **a** original, **b** degraded; **c** R-L; **d** RL-TV; **e** RL-FGP-1; **f** RL-FGP-2

Table 2 Cell image restoration evaluation

Images	ISNR	UIQI	#Passband	#Iter.
Degraded image	–	0.30	251	–
RL	1.14	0.42	1717	298
RL-TV $\lambda = 0.003$	2.16	0.48	3183	334
RL-FGP-1 (median)	2.43	0.54	5291	328
RL-FGP-2 (mean)	2.41	0.51	5291	325

(that is more noisy than image 2), the TV regularization performed slightly better in radial direction (x, y) as can be seen in Fig. 9 but not in axial direction as can be seen in Fig. 11, where the proposed method (RL-FGP-2) obtained a sharper result withouth oversmoothing the structures. The results obtained with RL-TV, RL-FGP-1, and RL-FGP-2 for the Real Image 2 (Fig. 10 and Table 4) where similar.

By changing the size of the original spectral support, it is possible to obtain a smoother result. An undesirable effect of this practice is the generation of ringing artifacts when the spectral support is taken to be too small. The performance (ISNR) and number of iterations as a function of the size of the frequency domain support is shown in Fig. 12. It can be observed that the quality of the result can be improved with minor changes in the support size, but it can also be degraded, specially when the support is shrinked.

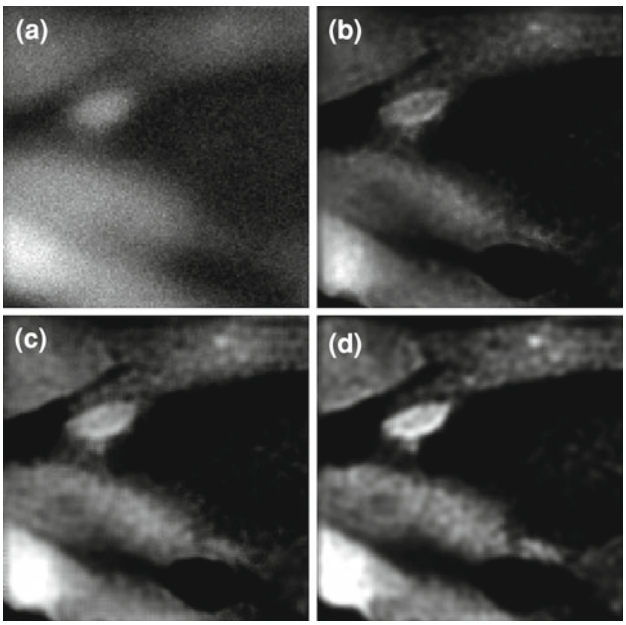

Fig. 9 A detail of sections $(x, y, 14)$ of the best restoration results for the real image 1: **a** degraded; **b** R-L; **c** RL-TV; **d** RL-FGP-2

There was no significant difference on the results when using a median or a mean filter in the filtering step. We believe it was because the filters are simple and used a small kernel.

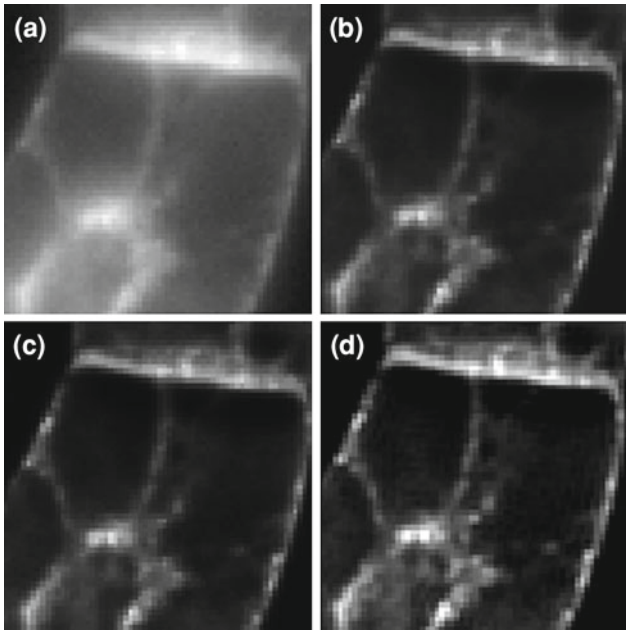

Fig. 10 A detail of sections $(x, y, 62)$ of the best restoration results for the real image 2: **a** degraded; **b** R-L; **c** RL-TV; **d** RL-FGP-2

Table 3 Real image 1 band extrapolation

Images	#Passband	#Iter.
Degraded image	311	–
RL	1179	225
RL-TV $\lambda = 0.005$	1465	286
RL-FGP-1 (median)	1271	270
RL-FGP-2 (mean)	1211	263

Table 4 Real image 2 band extrapolation

Images	#Passband	#Iter.
Degraded image	117	–
RL	2187	105
RL-TV $\lambda = 0.003$	2483	182
RL-FGP-1 (median)	2745	116
RL-FGP-2 (mean)	2731	117

The number of iterations needed to reach the conditions of the stop criterion using RL-FGP were similar to those of the R-L-TV method. In Fig. 13, it is possible to observe the ISNR as a function of the iterations for the image Bead, where the lines shows how the methods converges (or diverges) on a poor signal-to-noise ratio condition. The R-L method starts to diverge after some iterations and, therefore, the restoration is stopped earlier, while with regularization and the proposed methods the convergence is stable.

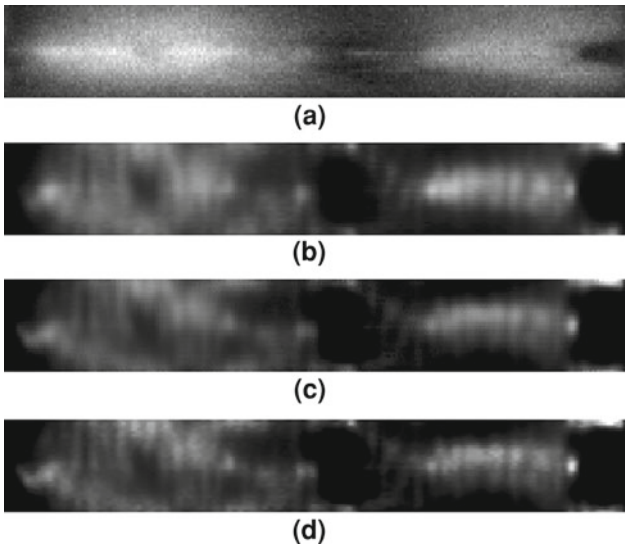

Fig. 11 Axial direction sections $(128, y, z)$ of the best restoration results for the real image 1: **a** degraded; **b** R-L; **c** RL-TV; **d** RL-FGP-2

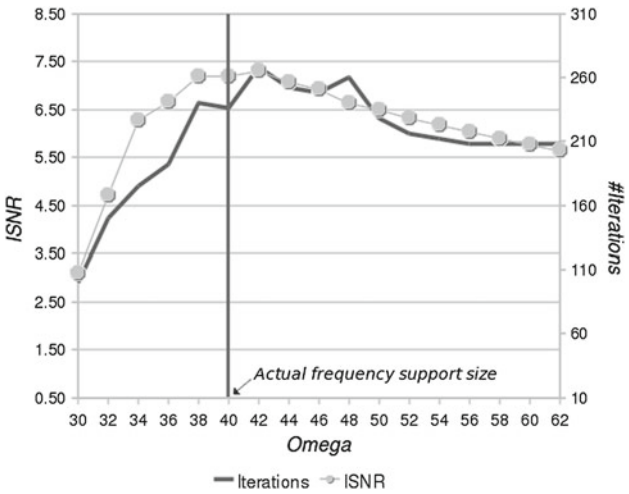

Fig. 12 ISNR and number of iterations as a function of the Ω parameter (image bandwidth) for bead image results of RL-FGP-1, where values in x axis represents the change in the frequency support size, and in y axis the performance in tems of ISNR (*left*) and number of iterations needed to complete the restoration (*right*)

8 Conclusion

Noise is always a difficult obstacle to overcome. Many well-known restoration algorithms yield good results in the absence of noise, but show poor performance when dealing with noisy data. The proposed algorithm performs a good restoration and frequency enhancement using constraints and filtering. The spatial support constraint allows a better spectral match to the original object and the filtering prevents noise amplification, stabilizing the result. It can be explained by the extra regularization included in the frequency domain due to the filtering step. The experiments with the real images

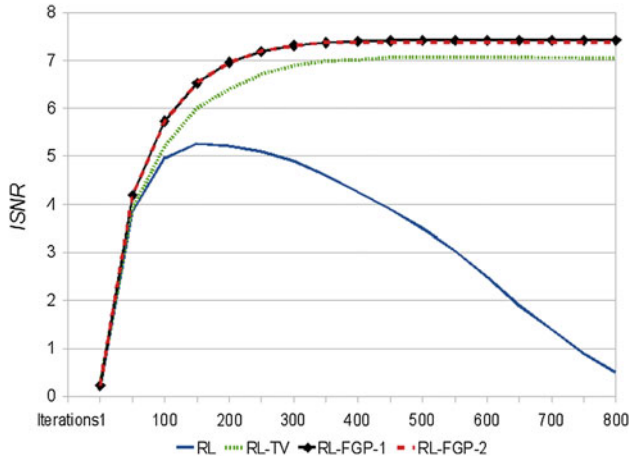

Fig. 13 ISNR as a function of the iterations for the methods R-L, RL-TV, RL-FGP-1 and RL-FGP-2 for the image Bead

also shown good results. However, the Total Variation regularization can perform better when restoring noisy and less blurred images such as confocal microscopy images.

The main contribution of this paper was to show that improved restoration can be achieved through a filtered extrapolation step combined with iterative restoration, with good potential to solve the described issues. Still, the band extrapolation in three-dimensional images remains an open problem, specially in the presence of noise.

Future research could investigate how the spectrum is restored by the RL-FGP as a function of the iterations, and how reliable is the achieved extrapolation. The pre-processing of the background as suggested by Ponti-Jr. and Mascarenhas [26], and the design of more accurate filters for selected frequency components, are also points left for future work.

Acknowledgments The authors would like to thank Prof. Murillo R. P. Homem for providing data and fruitful discussions. We are also grateful to the reviewers for the valuable suggestions.

References

1. Andrews, H.C., Hunt, B.R.: Digital Image Restoration, 2nd edn. Prentice-Hall, Englewood (1977)
2. Bhattarcharjee, S., Sundareshan, M.: Mathematical extrapolation of image spectrum for constraint-set design and set-theoretic superresolution. J. Opt. Soc. Am. A **20**(8), 1516–1527 (2003)
3. Bonettini, S., Zanella, R., L., Zanni, L.: A scaled gradient projection method for constrained image deblurring. Inverse Problems **25**, 015,002 (2009)
4. Colicchio, B., Haeberle, O., Xu, C., Dieterlen, A., Jung, G.: Improvement of the LLS and MAP deconvolution algorithms by automatic determination of optimal regularization parameters and pre-filtering of original data. Opt. Commun. **224**, 37–49 (2005)
5. Conchello, J.A.: Superresolution and convergence properties of the expectation-maximization algorithm for maximum-likelihood deconvolution of incoherent images. J. Opt. Soc. Am. A **15**(10), 2609–2619 (1998)
6. Danuser, G.: Super-resolution microscopy using normal flow decoding and geometric constraints. J. Microscopy **204**(2), 136–149 (2001)
7. Denney, T. Jr., Reeves, S.: Bayesian image reconstruction from fourier-domain samples using prior edge information. J. Electron. Imaging **14**(4), 043,009 (2005)
8. Dey, N., Blanc-Feraud, L., Zimmer, C., Roux, P., Kam, Z., Olivo-Marin, J.C., Zerubia, J.: Richardson-Lucy algorithm with total variation regularization for 3D confocal microscope deconvolution. Microsc. Res. Tech. **69**(4), 260–266 (2006)
9. Ferreira, P.: Interpolation and the discrete Papoulis-Gerchberg algorithm. IEEE Trans. Signal Process. **42**(10), 2596–2606 (1994)
10. Figueiredo, M., Bioucas-Dias, J.: Restoration of poissonian images using alternating direction optimization. IEEE Trans. Image Process. **19**, 3133–3145 (2010)
11. Foi, A., Bilcu, R., Katkovnik, V., Egiazarian, K.: Adaptive-size block transforms for signal-dependent noise removal. In: Proc. 7th Nordic Signal Processing Symposium (NORSIG'2006). Reykjavik, Iceland (2006)
12. Foi, A., Katkovnik, V., Egiazarian, K.: Pointwise shape-adaptive DCT for high-quality denoising and deblocking of grayscale and color images. IEEE Trans. Image Process. **16**(5), 1395–1411 (2007)
13. Gerchberg, R.: Super-resolution through error energy reduction. Opt. Acta **21**, 709–720 (1974)
14. Gibson, F., Lanni, F.: Experimental test of an analytical model of aberration in an oil-immersion objective lens used in three-dimensional light microscopy. J. Opt. Soc. Am. A **8**(11), 1601–1613 (1991)
15. Goodman, J.: Introduction to Fourier Optics, 2nd edn. McGraw Hill, New York (1996)
16. Homem, M., Mascarenhas, N., Costa, L., Preza, C.: Biological image restoration in optical-sectioning microscopy using prototype image constraints. Real Time Imaging **8**, 475–490 (2002)
17. Homem, M.R.P.: Reconstrução tridimensional de imagens com o uso de deconvolução a partir de seções bidimensionais obtidas em microscopia óptica (in portuguese). Doutorado em Física Computacional, Universidade de São Paulo - Instituto de Física de São Carlos (2003)
18. Hunt, B.: Super-resolution of images: algorithms, principles, performance. Int. J. Imaging Syst. Technol. **6**, 297–304 (1995)
19. van Kempen, G., van Vliet, L., Verveer, P.: Application of image restoration methods for confocal fluorescence microscopy. In: Cogswell, C., Conchello, J.A., Wilson, T. (eds.) 3-D Microscopy: Image Acquisition and Processing IV, vol. 2984, pp. 114–124. SPIE, Washington (1997)
20. Kenig, T., Kam, Z., Feuer, A.: Blind image deconvolution using machine learning for three-dimensional microscopy. IEEE Trans. Pattern Anal. Mach. Intell. **32**(12), 2191–2204 (2010) (in press)
21. Lippincott-Schwartz, J., Patterson, G.: Development and use of fluorescent protein markers in living cells. Science **300**(5616), 87–91 (2003)
22. Lucy, L.: An iterative technique for the rectification of observed distributions. Astron. J. **79**(6), 745–765 (1974)
23. Malgouyres, F., Guichard, F.: Edge direction preseving image zooming: a mathematical and numerical analysis. SIAM J. Numer. Anal. **39**(1), 1–37 (2001)
24. Papoulis, A.: A new algorithm in spectral analysis and band-limited extrapolation. IEEE Trans. Circuit. Syst. **22**(9), 735–742 (1975)
25. Philip, J.: Optical transfer function in 3d for a large numerical aperture. J. Mod. Opt. **46**(6), 1031–1042 (1999)
26. Ponti-Jr., M.P., Mascarenhas, N.: Does background intensity estimation influence the restoration of microscopy images? In: IEEE Proceedings 23rd SIBGRAPI—Conference on Graphics, Patterns and Images. IEEE (2010)

27. Ponti-Jr., M.P., Mascarenhas, N., Suazo, C.: A restoration and extrapolation iterative method for band-limited fluorescence microscopy images. In: IEEE Proceedings XX Brazilian Symposium on Computer Graphics and Image Processing, pp. 271–280. IEEE (2007)
28. Restrepo, A., Chacon, L.: A smoothing property of the median filter. IEEE Trans. Signal Process. **42**(6), 1553–1555 (1994)
29. Richardson, W.: Bayesian-based iterative method of image restoration. J. Opt. Soc. Am. **62**(1), 55–59 (1972)
30. Sarder, P., Nehorai, A.: Deconvolution methods for 3-D fluorescence microscopy images. IEEE Signal Process. Mag. **23**(3), 32–45 (2006)
31. Sawicki, J.: Median algorithms—characterized in frequency domain. In: Proceedings of IEEE International Symposium Intelligent Signal Processing, pp. 203–207 (2003)
32. Sementilli, P., Hunt, B., Nadar, M.: Analysis of the limit to superresolution in incoherent imaging. J. Opt. Soc. Am. A **10**, 2265–2276 (1993)
33. Sheppard, C., Gu, M., Kawata, Y., Kawata, S.: Three-dimensional transfer functions for high-aperture systems. J. Opt. Soc. Am. A **11**(2), 593–598 (1994)
34. Snyder, D., Miller, M.: Random Point Processes in Time and Space. Springer, Berlin (1991)
35. Song, L., Hennink, E., Young, I., Tanke, H.: Photobleaching kinetics of fluorescein in quantitative fluorescence microscopy. Biophys. J. **68**, 2588–2600 (1995)
36. Wang, Z., Bovik, A.: A universal image quality index. IEEE Signal Process. Lett. **9**(3), 81–84 (2002)